


Fast dispersion tailoring of multimode photonic crystal resonators

Francesco Rinaldo Talenti ^{1,2,*} Stefan Wabnitz,^{1,3} Inès Ghorbel,² Sylvain Combrié,²
Luca Aimone-Giggio,² and Alfredo De Rossi²

¹*Dipartimento di Ingegneria dell'Informazione, Elettronica e Telecomunicazioni, Sapienza University of Rome, 00184 Rome, Italy*

²*Thales Research and Technology, Campus Polytechnique, 1 Avenue Augustin Fresnel, 91767 Palaiseau, France*

³*CNR-INO, Istituto Nazionale di Ottica, Via Campi Flegrei 34, 80078 Pozzuoli, Italy.*



(Received 11 May 2022; revised 18 July 2022; accepted 20 July 2022; published 4 August 2022)

We introduce a numerical procedure which permits us to drastically accelerate the design of multimode photonic crystal resonators. Specifically, we demonstrate that the optical response of an important class of such nanoscale structures is reproduced accurately by a simple, one-dimensional model within the entire spectral range of interest. This model can describe a variety of tapered photonic crystal structures. Orders of magnitude faster to solve, our approach can be used to optimize certain properties of the nanoscale cavity. Here we consider the case of a nanobeam cavity, for which the confinement results from the modulation of its width. The profile of the width is optimized in order to flatten the resonator dispersion profile (so that all modes are equally spaced in frequency). This result is particularly relevant for miniaturizing parametric generators of nonclassical light, optical nanocombs, and mode-locked laser sources. Our method can be easily extended to complex geometries, described by multiple parameters.

DOI: [10.1103/PhysRevA.106.023505](https://doi.org/10.1103/PhysRevA.106.023505)

I. INTRODUCTION

The nonlinear interaction among several resonant fields in an optical resonator leads to efficient Raman and Brillouin scattering, three- and four-wave mixing, optical parametric oscillation [1], laser mode locking, and frequency-comb generation [2]. Scaling down the size of optical resonators implies that the optical power level for triggering nonlinear effects decreases as V^{-1} or V^{-2} , where V is an effective volume of the spatial distribution of the interacting fields. In the context of photonic integration, the decrease in the power budget is of paramount importance.

Nanoscale optical resonators such as photonic crystals are able to confine light within $V \approx \lambda^3$, i.e., a wavelength-sized volume, with a photon decay time, or interaction time, well above 1 ns (i.e., the cavity quality factor $Q \gg 10^6$). Owing to these properties, it has been possible to demonstrate nanoscale lasers [3–6], Raman sources [7], and, more recently, optical parametric oscillators [8], all operating with a power supply (optical or electrical) in the microwatt range. Yet a major challenge remains in achieving the nonlinear interaction of multiple longitudinal modes, as it occurs in mode-locked lasers or in microcombs. While ring or microdisk resonators naturally provide the necessary, nearly frequency-equispaced set of cavity resonances, achieving the same condition in nanoscale resonators is notoriously a nontrivial task. On the other hand, nanoscale resonators could, in principle, be designed in a way that a specified number of modes, starting from the fundamental mode, are allowed to take part in the nonlinear interaction. This unique property not only implies

that a much higher degree of control of power transfer among modes (which is crucial in quantum and signal processing applications [9]) can be achieved, but also leads to maximizing the interaction efficiency. This is because, in the typical configuration of a nanoscale resonator, the lowest-order modes are also the most tightly confined. Moreover, in a mode-locked nanolaser, the control of the interacting modes would enable a favorable scaling of the repetition rate vs the size of the device [10].

It has been shown that some specific designs of a photonic crystal cavity lead, for some set of parameters, to frequency-equispaced eigenmodes; moreover, their mode envelopes are described by Hermite-Gauss functions. This suggests that, within a certain spectral range, the complex photonic crystal structure can be well approximated by a quantum-mechanical harmonic oscillator model [11,12]. It has also been shown that postfabrication trimming is effective in correcting for fabrication tolerances, thereby demonstrating an almost perfect alignment of the cavity resonances [13]. Yet a systematic design approach for generating a given number of equispaced modes, or, more generally, with a prescribed dispersion profile, while at the same time maximizing the radiation-limited Q factor is still missing, while brute-force methods are extremely inefficient.

Finding a cavity geometry, or, more generally, a physical system whose response to an input excitation corresponds to a well-defined target function, e.g., a spatial distribution of the dielectric permittivity such that the electromagnetic field has prescribed resonances, belongs to the class of *inverse problems*, which are notoriously difficult to solve. Yet progress in nanofabrication techniques has motivated the development of powerful methods such as topological optimization (TO) [14] and inverse design (ID) [15]. The common feature of these

*Corresponding author: francescorinaldo.talenti@uniroma1.it

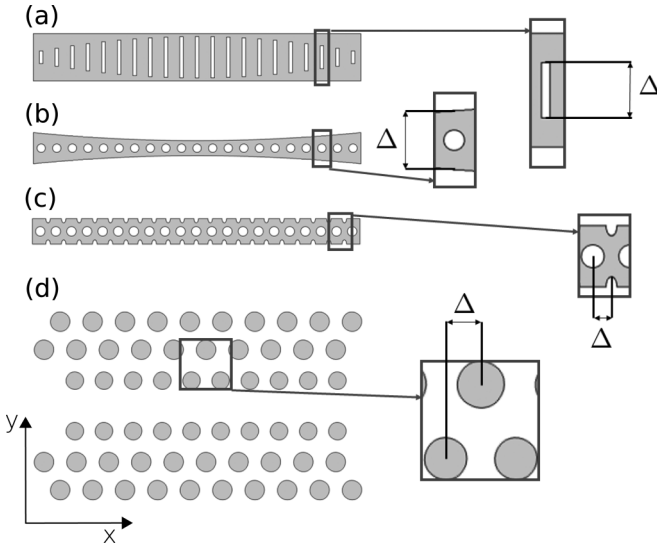


FIG. 1. Common design of high- Q resonators based on *gentle* confinement: (a) tapered distributed feedback grating [18], (b) 1D nanobeam with parabolic width [25], (c) 1D nanobeam bichromatic resonator [26], and (d) two-dimensional bichromatic resonator [11] and the corresponding tapering parameter Δ .

two approaches is that their result is a spatial distribution of $\varepsilon(\mathbf{x})$, rather than an optimized set of parameters for a predefined geometry. These methods are therefore able to *create* novel geometries, hence the reference to *design*. Moreover, automatic differentiation [16] and the adjoint method [17] enable a very efficient computation of the gradient, which is required in the iterative search of the optimum distribution, even in the presence of nonlinearity.

Here we follow a radically different approach, which is arguably more suited for the class of problems under consideration. This is motivated by the fact that the geometries of nanoscale resonators with the largest experimentally reported Q factors [18–22] are still based on the principle of *gentle confinement* [23]. In other words, these nanostructures are essentially periodic, with an adiabatic tapering of some parameters, i.e., a gentle change in the radius of the holes, the period, or the magnitude of a “dislocation” defect. We note that more aggressive design strategies, including TO and ID, have instead been considered for different tasks, e.g., for maximizing light-matter interactions in *single-mode* resonators [16,24].

Let us restrict our search to a family of structures which can be described by means of a periodic pattern $\varepsilon(\mathbf{x}, \Delta)$ that depends on a *control* parameter Δ , which is supposed to adiabatically vary in space (i.e., *gently*). Some examples of such geometries are given in Fig. 1. The crucial point is that it is possible to map the three-dimensional (3D) Maxwell equations (MEs) into an equivalent system of one-dimensional (1D) equations, which will be referred to as the *reduced model* (RM). Remarkably, the relative precision of the resonances predicted by the RM turns out to be at least as good as the precision of the direct numerical solution of the 3D ME. The search for the desired optimal spatial dependence of Δ will be performed by using any suitable optimization method, leveraging the extremely faster solution of the RM

when compared the direct solution of the 3D MEs. The RM itself requires only a single direct solution of the 3D MEs for building an initial approximation of the structure. Subsequent applications of the RM are used in order to refine the first approximation. As we shall see, in total only three 3D solvers are sufficient for obtaining a design that matches our target with an accuracy that is equivalent to that of directly solving the 3D MEs but with a comparatively much larger number of iterations.

Hereafter we will first discuss the derivation of the RM; then we will formulate a design target, followed by the introduction of the optimization procedure, including model calibration. Finally, we will discuss possible applications and generalizations of the model.

II. REDUCED MODEL FOR A PERIODIC PHOTONIC CRYSTAL

The reduced model is inspired by the so-called $\mathbf{k} \cdot \mathbf{p}$ method [27], which is used in solid-state physics to model the electronic band structure of crystals. The main idea of the method is to describe the dispersion relation of the electronic bands (i.e., electron energy vs wave vector \mathbf{k}) through a suitable algebraic equation, which is built upon the eigenfunctions of the exact Hamiltonian at the bands’ extrema (at points of high symmetry, e.g., $\mathbf{k} = 0$, or the Γ point). Within a range of energies of interest, the dispersion relation is extrapolated from the Γ point by treating the $\mathbf{k} \cdot \mathbf{p}$ term as a perturbation. In this way, the complexity of solving the full Schrödinger equation for the crystal is reduced by using a much simpler model in which only a few parameters need to be suitably adjusted. As a consequence of this approach, the local modulation of a semiconductor, e.g., of a heterostructure, can be well described in terms of a change in these parameters within the energy range of interest. As a result, it is possible to introduce a much simpler Schrödinger equation which depends only on these parameters.

In optics, the simplest model for describing the propagation of waves in a periodic dielectric is provided by the distributed Bragg reflector. Here a modulation with period Λ of the dielectric permittivity couples forward and backward waves. A simple algebraic equation approximates the dispersion in the spectral range that is centered at the Bragg angular frequency $\omega_0 = \pi c_0 n^{-1} \Lambda^{-1}$. Here c_0 is the speed of light in vacuum, and n is an effective refractive index which describes the optical-field distribution as a result of the dielectric inhomogeneity [28]. In the presence of an intensity-dependent contribution to the refractive index, one obtains coupled wave-propagation equations which generalize the massive Thirring model of field theory; their solitary wave solutions (gap or Bragg solitons) describe the localization of wave packets in periodic media [29]. The simplicity of the gap-soliton model has facilitated the study of soliton stability by using analytical criteria [30]. Soliton dynamics has been experimentally demonstrated in nanoscale photonics [31], and it has been shown that nonlinear coupled-wave models are able to fully capture the underlying physics [32]. Hereafter, we will consider only a generalized linear version of the gap-soliton model, and demonstrate that the model accurately describes

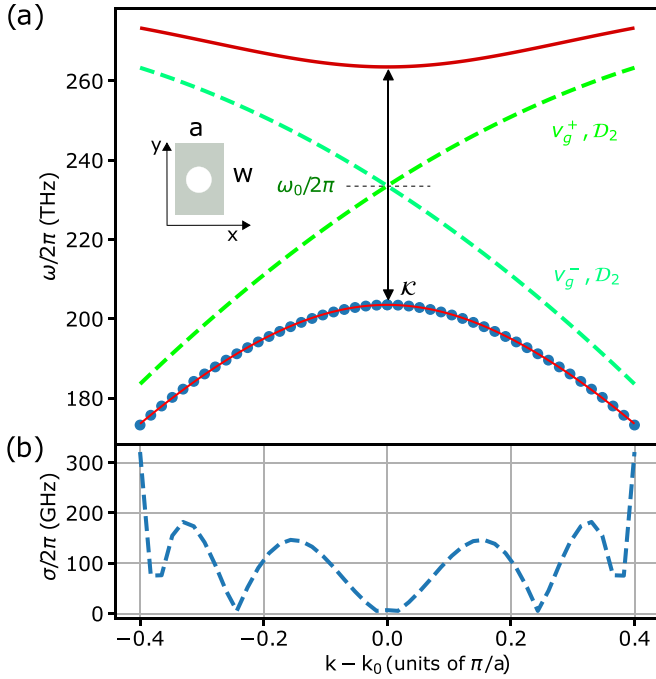


FIG. 2. (a) Dispersion diagram of a periodic structure (see inset) with width $w = 450$ nm and period $a = 465$ nm, centered on the K point of the reduced Brillouin zone ($k_0 = \pi/a$). The reduced model considers coupled forward and backward waves (dashed lines), generating the valence and conduction bands (solid lines). The solid circles represent the valence band calculated by periodic 3D MEs. (b) The corresponding residuals $\sigma/2\pi$ of the fit.

wave propagation in adiabatically modulated photonic crystal structures.

Let us consider two counterpropagating waves $E^\pm(x, t) = A_k^\pm \exp(i\omega t \pm ikx)$, with group velocity v_g , coupled by a periodic modulation of the dielectric permittivity with scaled magnitude \mathcal{K} . In the presence of this linear coupling, the dispersion relation of the waves is described by the coupled equations

$$\begin{aligned} (v_g k + \mathcal{D}_2 k^2 + \omega_0) A_k^+ + \mathcal{K} A_k^- &= \omega A_k^+, \\ (-v_g k + \mathcal{D}_2 k^2 + \omega_0) A_k^- + \mathcal{K} A_k^+ &= \omega A_k^-. \end{aligned} \quad (1)$$

Let us note that we introduced the Bragg angular frequency ω_0 and added the second-order dispersion term \mathcal{D}_2 . The set $\{\omega_0, \mathcal{K}, v_g, \mathcal{D}_2\}$ describes the dispersion of the coupled waves, and we will refer to it as the *structure parameters*. We now derive these parameters for periodic structures with different widths w by focusing on a specific portion of the dispersion relation, namely, one or more bands, as shown in Fig. 2(a).

Here we consider a so-called nanobeam photonic crystal, where the width w of the beam takes the role of the control parameter [Fig. 1(b)]. The nanobeam is supposed to be made out of a III-V-group semiconductor alloy $\text{In}_{0.5}\text{Ga}_{0.5}\text{P}$, with refractive index $n = 3.17$. The nanobeam is $h = 180$ nm thick, with a $w = 450$ nm width and an $a = 465$ nm period; the hole radius is $0.27a$. The valence band $\omega_v(k)$ is obtained by solving the 3D MEs with Bloch periodic boundary conditions along

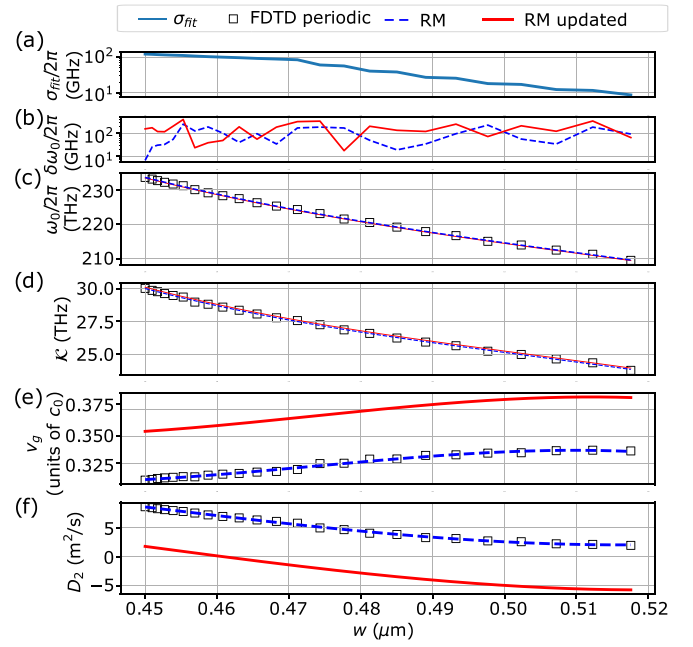


FIG. 3. Calculated structural parameters for the RM vs the control parameter w . (a) Averaged residual of the fit and (c)–(f) extracted parameters (black squares), polynomial fit (blue dashed line), and polynomial fit on the updated RM (solid red line). In (e) the group velocity is reported in units of c_0 , i.e., the speed of light in vacuum. (b) Residual of the fit of ω_0 (dashed blue line) and after updating the RM (red solid line).

x , i.e., $\mathbf{E}_k(\mathbf{r} + a\hat{x}) = E_k(\mathbf{r}) \exp(ika)$. This is performed by means of the periodic finite-difference time-domain (FDTD) algorithm with a perfectly matched layer placed at the z and y boundaries. The parameters are adjusted in order to minimize the error $N^{-1} \sum_{k_i=0}^{N-1} \sigma^2(k_i)$ over the N points in the reciprocal space, with $\sigma^2(k_i) = [\omega_v(k_i) - \omega_v^{(\text{RM})}(k_i)]^2$ obtained from the reduced model $\omega_v^{(\text{RM})}$, i.e., the characteristic equation solutions of the linear system Eq. (1). This generates the set of parameters $\{\omega_0, \mathcal{K}, v_g, \mathcal{D}_2\}(w)$, which depends on the control parameter w . The average of the residual error in the reciprocal-space region of interest $\sigma_{\text{fit}} = \sigma(k)$ is about 100 GHz, [see Fig. 2(b)]. Let us note that this error is about the same as the estimated discretization error of the FDTD method [33]. This point is further discussed in the Appendix.

Figure 3 describes the dependence of the structure parameters on the control parameter w . Figure 3(a) shows that the fit error decreases when w grows from 0.45 to 0.52 μm , meaning that the dispersion relation is increasingly closer to that of the RM. In Figs. 3(c)–3(f), the blue dashed line represents the polynomial fit of the extracted parameters with respect to w . Here we make a crucial assumption, namely, that the dependence of the structure parameters on w is smooth. Figure 3 shows that a low-order (third) polynomial is a good approximation; moreover, the residual of ω_0 [blue solid line in Fig. 3(b)] is about 100 GHz or less. The result here is a set of polynomial coefficients $C_i^{(\mathcal{P})}$ for each parameter $\mathcal{P} = \{\omega_0, \mathcal{K}, v_g, \mathcal{D}_2\}$. This two-step interpolation of the dispersion of the periodic structure removes the minute deviations which might be related to the discretization error.

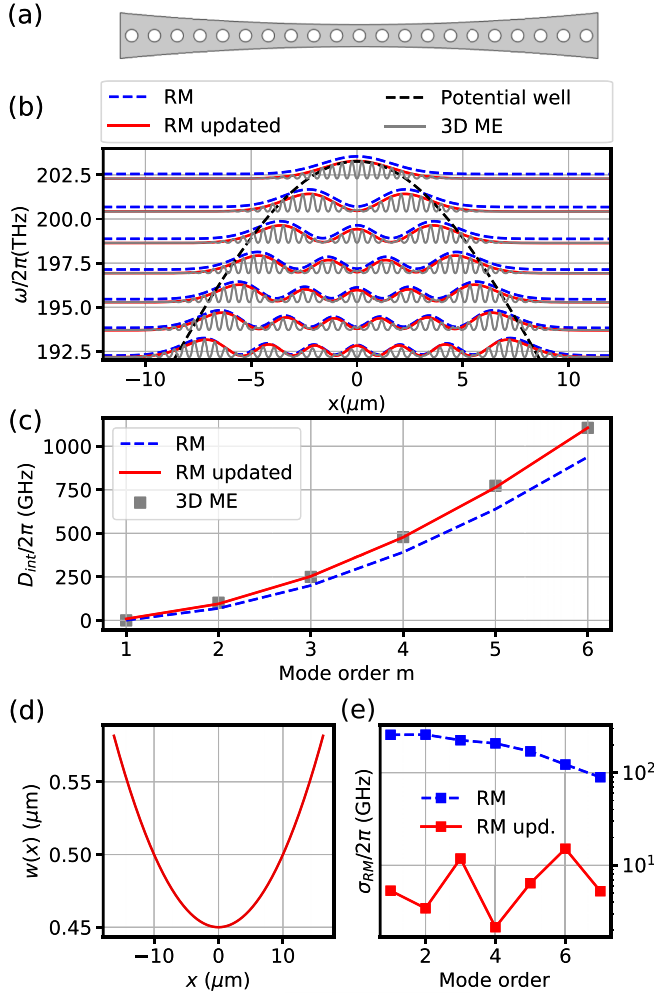


FIG. 4. Tapered nanobeam optical cavity. (a) Simplified layout and (b) spatial dependence of the valence band edge at $k = k_0$ (dashed black line), the normalized distribution of the squared electric field corresponding to the calculated Bloch modes (3D MEs) of the cavity along the axis $y = 0$, $z(d) = 0$ (solid gray line), and envelopes calculated from the reduced model of the cavity (blue dashed line) and after the model update (red solid line). The vertical offset corresponds to the frequency at resonance. (c) Integrated dispersion D_{int} calculated by solving the 3D MEs (squares), with the reduced cavity model (blue dashed line) and after the update (red solid). (d) Spatial dependence of w . (e) Frequency deviation for each mode $\sigma_{\text{RM}}/2\pi$ of the RM (blue dashed line) and the updated RM (red solid line) relative to the 3D ME calculations.

III. REDUCED MODEL OF A TAPERED NANOBEAM CAVITY

Let us now consider an optical resonator where the confinement is due to the tapering of the width $w(x) = \rho_0 + \rho x^2$ ($\rho > 0$) of the nanobeam, as described in Ref. [25]. When considering the w dependence of ω_0 and \mathcal{K} in Fig. 3(d), we immediately realize that the edge of the valence band $\omega_{vb} = \omega_0 - \mathcal{K}$ decreases as w increases. This leads to localization of Bloch waves in the valence band of the nanobeam if w is smaller in the center of the nanobeam. Let us consider the case with $\rho = 500 \text{ m}^{-1}$. Figure 4(b) shows the corresponding spatial distribution of the modes as it is obtained from the

solution of the 3D MEs using the finite-element method (details are discussed in the Appendix).

Let us now build a RM for the cavity and define the linear operator \mathcal{L}_{RM} acting on complex-valued functions of space x ($\mathcal{R} \rightarrow \mathcal{R}^2$):

$$\mathcal{L}_{\text{RM}} = \begin{bmatrix} -\mathcal{D}_2 \partial_x^2 + i v_g \partial_x + \omega_0 & \mathcal{K} \\ \mathcal{K} & -\mathcal{D}_2 \partial_x^2 - i v_g \partial_x + \omega_0 \end{bmatrix}. \quad (2)$$

Here the structure parameters $\{\omega_0, \mathcal{K}, v_g, \mathcal{D}_2\}$ are all functions of x via the profile $w(x)$ and the polynomials $\mathcal{C}_i^{(\mathcal{P})}$. Namely, for each parameter \mathcal{P} the corresponding function of x reads

$$\mathcal{P}(x) = \sum_l \mathcal{C}_l^{(\mathcal{P})} w(x)^l. \quad (3)$$

The polynomial expansion is replaced by constant values for $|x| > x_{\text{max}}$, namely, $\mathcal{P}|_{|x| > x_{\text{max}}} = \mathcal{P}(x_{\text{max}})$. The eigenfunctions $\psi = [\mathcal{A}^+, \mathcal{A}^-]$ of the equation

$$(\mathcal{L}_{\text{RM}} - \omega)\psi = 0 \quad (4)$$

correspond to the envelopes of the cavity modes, as predicted by the RM. The equation is solved by finite-difference discretization (see the Appendix). It is apparent that the field envelopes and the eigenfrequencies are close to the corresponding results from a direct solution of the 3D MEs. A very important figure to describe the dispersion in multimode resonators is the integrated dispersion [2], which measures the deviation of the cavity resonances ω_m from a constant free spectral range (FSR): $D_{\text{int},m} = \omega_m - \omega_0 - \mathcal{D}_1 m$. This quantity is shown in Fig. 4(c). The FSR is fixed to $\mathcal{D}_1 = \omega_1 - \omega_0$ from the solution of the 3D MEs, where ω_0 is always the first eigenvalue (the fundamental mode); this implies that we consider only the relative error of the eigenvalues between the 3D ME results and the RM predictions. Let us also note that the modes are ordered with decreasing frequency because the valence band has an upper bound. The deviation $\sigma_m = |\omega_m(3\text{D MEs}) - \omega_m(\text{RM})|$ is shown in Fig. 4(e): as can be seen, its value is about 100 GHz. Let us now allow the polynomial coefficients \mathcal{C}_i to be adjusted in order to minimize the mismatch between the eigenfrequencies obtained from the solution of the 3D MEs and from the RM, namely,

$$\epsilon = \frac{1}{N} \sum_m \left| \frac{\sigma_m}{\omega_0} \right|^2. \quad (5)$$

The results correspond to the red lines in Fig. 4(b), which are now much closer to the Bloch modes obtained from the solution of the 3D MEs. This is even more visible when inspecting D_{int} [Fig. 4(c)] and the corresponding residual [Fig. 4(e)], which is now below 10 GHz. Let us now analyze the change in the polynomial coefficients by inspecting the change in the dependence of \mathcal{P} on w in Figs. 3(b)–3(f). The relative change in the parameters is very small and merely appears as an offset. The relative change in \mathcal{D}_2 is larger, but this parameter represents a higher-order correction to the coupled-wave model. Thus, a slight adjustment of the parameters is sufficient to let our reduced model converge to the solution of the 3D MEs. We will refer to it hereafter as the “updated” RM. The fact that a correction of the parameters is needed is justified by the fact that the adiabatic condition for the tapering is only

partially satisfied. Yet it is noteworthy that the RM already generates a very good approximation of the numerically exact result, and that a slight change in the polynomial coefficients is enough to match the exact result within the discretization error in the solution of the 3D ME. The updated RM solution is, in this sense, fully equivalent to the 3D ME solution.

IV. DESIGN OF A MULTIMODE RESONATOR WITH A FLAT DISPERSION

Let us now consider the updated RM, which consists of the eigenvalue Eq. (4) with the operator Eq. (2) and parameters defined by the updated coefficients C_i . The profile $w(x)$ is now allowed to change, so that the integrated dispersion D_{int} converges towards a prescribed target. As a notable example, we consider a flat dispersion profile for the first seven modes as a target, i.e., $D_{\text{int},m} = 0$ for $m = 1, \dots, 7$. The tapering profile is defined by a polynomial with even orders up to $2M = 6$: $w(x) = \rho_0 + \sum_{l=1}^M \rho_l x^{2l}$. With this choice we have three degrees of freedom in the optimization process (ρ_l , with $l = 2, 4, 6$), ensuring both convergence and high computational efficiency. The cost function $\sum_m |D_{\text{int},m}|$ is minimized with respect to the parameters ρ_l . This results in a new profile $w_1(x)$ [Fig. 5(c)], for which the RM predicts that $D_{\text{int}}/2\pi$ decreases by almost 2 orders of magnitude to about 2–4 GHz [Fig. 5(b)]. The 3D MEs are solved again with $w_1(x)$, and the resulting $D_{\text{int}}/2\pi$ is reduced to about 10 GHz, i.e., not as much as the prediction of the RM. The coefficients C are updated such that RM approaches the 3D MEs, as in the previous section. This is necessary since $w_1(x)$ has considerably departed from a parabola. Indeed, Fig. 5(d) shows that the residuals (red dashed line) are larger than the estimated accuracy of the 3D MEs (green dashed line), yet they decrease below it after the second update (solid red line). A new optimized profile is then generated $w_2(x)$, yet no appreciable change is achieved [Figs. 5(b)–5(d)], indicating that the procedure has reached convergence, which is essentially set by the accuracy of the 3D ME solver. In summary, the method required solving once for the periodic 3D MEs and solving the 3D MEs twice more for the cavity; the third time only confirms convergence.

Finally, we analyze how the ID procedure affects the Q factors. Since our procedure does not consider Q a target for optimization, there is no guarantee that high- Q values are preserved. This is examined in Fig. 6. The Q factors have been calculated either deterministically (circles) or by modeling the fabrication imperfections by introducing disorder, i.e., by randomly varying (rms = 0.5 nm) the position and the diameter of all the holes. The error bars represent statistics (the mean value and the standard deviation of a log-normal distribution) over an ensemble of 20 simulations. Thus, circles correspond to the radiation-limited Q , which decreases Q to less than 10^6 after the optimization. Importantly, this is no longer true when disorder is taken into account, as Q factors are basically unchanged.

V. CONCLUSIONS

We have introduced a procedure for the inverse design of the dispersion of a multimode nanoscale resonator. The main idea behind our approach harnesses the fact that nanoscale

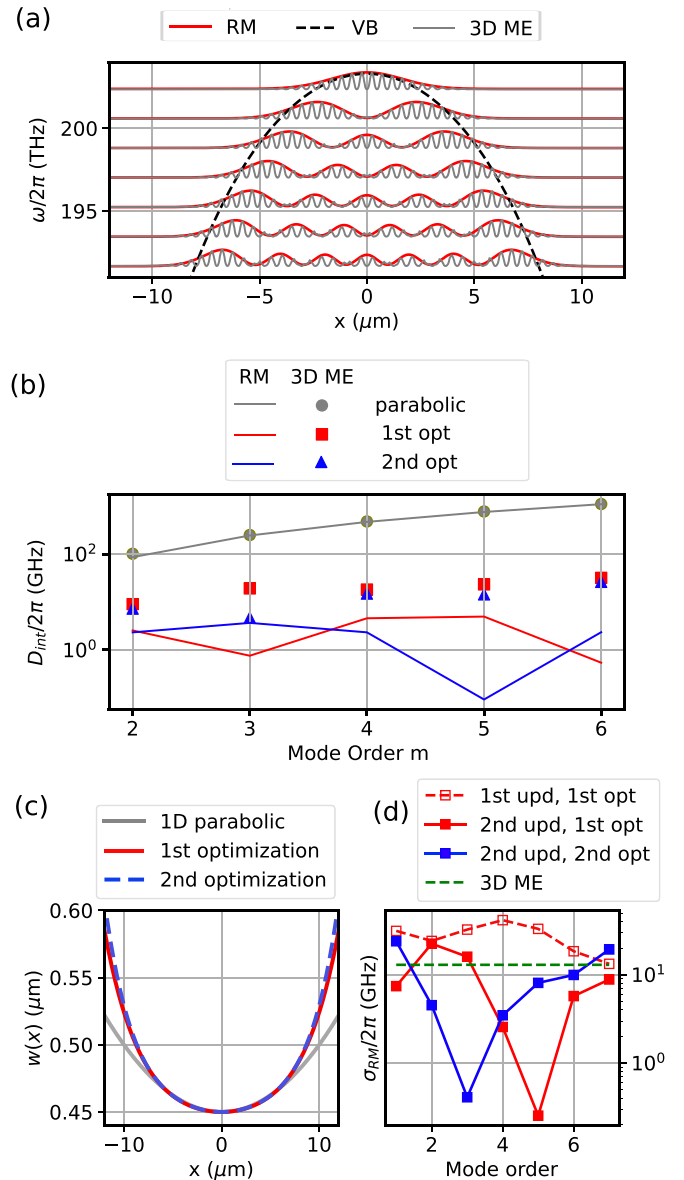


FIG. 5. Design of a nanobeam multimode resonator with flat dispersion. (a) Bloch modes (from the 3D ME) and envelopes from the RM after optimization (as in Fig. 4). (b) Integral dispersion D_{int} for the resonator with parabolic tapering $w_0(x)$ (gray) and after the first $w_1(x)$ (red) and second $w_2(x)$ (blue) optimizations. Symbols represent the solution of the 3D ME, and lines correspond to the RM solutions. Note the logarithmic vertical scale. (c) Corresponding tapering profiles $w_i(x)$. (d) Residuals (difference between RM and 3D MEs) computed after updating the RM with $w_0(x)$ (red dashed line), after the second update and $w_1(x)$ (red solid line), and with $w_2(x)$ (blue line).

cavities with large quality factors are, in general, designed according to the principle of “gentle confinement.” This implies that they can be described as almost adiabatically tapered periodic structures. Inspired by well-known methods of solid-state physics, we have introduced a reduced model which is able to capture very well the dispersion of the nanoscale structure in the spectral domain of interest, where the cavity modes exist. The reduced model consists of a linear operator acting on complex functions of a single variable, whose parameters

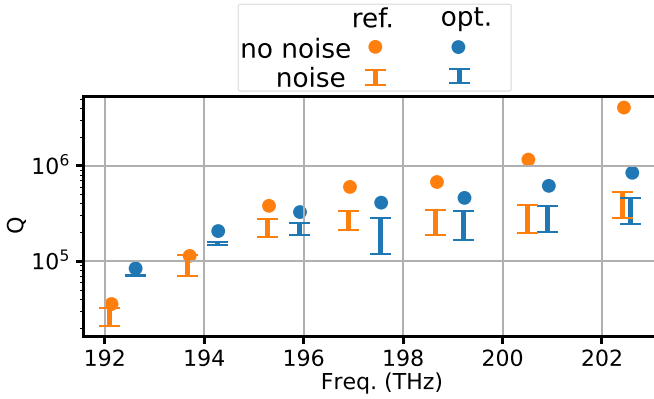


FIG. 6. Calculated Q factors for the reference cavity with parabolic tapering $w_0(x)$ (orange) and the dispersion-flattened cavity with an optimized profile (blue). Circles correspond to the radiation-limited Q ; error bars are an estimate of Q accounting for fabrication disorder. On the x axis the frequency of the resonances is reported.

are slowly varying. These parameters are initially determined by fitting the dispersion of a reference periodic structure via a function of the “control” parameter. Here we considered the case of a “nanobeam” photonic crystal cavity. The width of the nanobeam is decreased in the middle, which creates a confining potential in the valence band of the photonic crystal. Next, the model is updated by adapting the nanobeam parameters to the cavity. This two-step procedure avoids issues related to the possible presence of suboptimal minima in the fitting procedure. We showed that the reduced model is equivalent to the solution of the 3D Maxwell equations within the discretization accuracy of the numerical solver, but it is 3 orders of magnitude faster. For this reason, any optimization algorithm can be used. As an example, we considered the problem of flattening the dispersion of a nanoscale resonator. The integrated dispersion D_{int} is reduced below ~ 10 GHz, essentially limited by the numerical accuracy of the Maxwell solver.

Our method can be applied to any cavity geometry which can be described via the one- or two-dimensional tapering of a periodic structure. The model can be extended to use more than one control parameter and could also leverage the presence of multiple waves. In contrast to topological optimization or inverse design, which are intended to solve a very general class of problems, our procedure is particularly suited to a specific but important class of optical resonators, and could considerably help with the development of nanoscale optical combs, mode-locked lasers, and special-purpose parametric generators of nonclassical light.

ACKNOWLEDGMENTS

The project leading to this application received funding from the European Union’s Horizon 2020 research and innovation program under the Marie Skłodowska-Curie EID project “MOCCA” (Grant Agreement No. 814147), the ITN project “OPHELLIA” (Grant Agreement No. 101017136), and the ERC project “STEMS” (Grant Agreement No. 740355). The authors thank L. M. Massaro and F. Raineri for stimulating discussions.

APPENDIX

1. Numerical implementation

The reduced model requires the solution of the eigenvalue problem Eq. (1), which is a system of linear partial differential equations. This is solved by finite-difference discretization of the operator $\hat{\mathcal{L}}_{\text{RM}}$,

$$\hat{\mathcal{L}}_{\text{RM}} = \begin{bmatrix} \hat{\omega}_0 - \hat{D}_2 \hat{D}_x^2 + i \hat{v}_g \hat{D}_x^{\text{FW}} & \hat{\mathcal{K}} \\ \hat{\mathcal{K}} & \hat{\omega}_0 - \hat{D}_2 \hat{D}_x^2 - i \hat{v}_g \hat{D}_x^{\text{BW}} \end{bmatrix},$$

where the hat symbol in \hat{D}_2 and \hat{D}_x indicates the finite-difference approximation of the differential operators, i.e., a $2N \times 2N$ matrix, where N is the number of points used to approximate the spatial domain. Therefore, $\hat{\mathcal{L}}_{\text{RM}}$ is $4N \times 4N$ matrix. The operator \mathcal{L}_{RM} is generally non-Hermitian; thus, its eigensolutions are not real. Localized eigenfunctions correspond to nearly real eigenvalues ($\text{Re}\{\hat{\omega}\} \gg \text{Im}\{\hat{\omega}\}$). The difference operators \hat{D}_x^2 and $\hat{D}_x^{\text{FW,BW}}$ are implemented on a regular grid $x_j = j\Delta x$ using a second-order central difference scheme and third-order forward and backward upwind schemes [34,35],

$$\begin{aligned} \hat{D}_x^{\text{FW}} f_j &= \frac{-f_{j+2} + 6f_{j+1} - 3f_j - 2f_{j-1}}{6\Delta x}, \\ \hat{D}_x^{\text{BW}} f_j &= \frac{f_{j-2} - 6f_{j-1} + 3f_j + 2f_{j+1}}{6\Delta x}, \end{aligned} \quad (\text{A1})$$

and for the second-order derivative

$$D_x^2 f_j = \frac{f_{j+1} - 2f_j + f_{j-1}}{h^2}. \quad (\text{A2})$$

As the terms of the difference scheme outside the domain are implicitly set to zero, they imply Dirichlet boundary conditions, which are not appropriate to represent either evanescent field decay or dispersive waves. Therefore, the considered computation domain is much larger than the size of the cavity. The other operators are diagonal, $\hat{v}_g = \delta_{i,j} v_g(x_j)$, $\hat{\mathcal{K}} = \delta_{i,j} \kappa(x_j)$, and $\hat{\omega}_0 = \delta_{i,j} \omega_0(x_j)$, with $\delta_{i,j}$ being the Kronecker delta. All of the code written for optimization and evaluation of the reduced model is written in JULIA [36].

2. Numerical accuracy

A critical issue when calculating the dispersion of multimode nanoscale cavities is that the relative error in the calculation of frequencies can hardly decrease below 10^{-4} , which translates to inaccuracies of the order of tens of gigahertz. In Ref. [33] a variety of methods for solving the ME are compared for computing the resonances of a nanoscale cavity. It was observed that finite-element methods (FEMs) converge better than finite-difference time-domain (FDTD) methods. Yet it was concluded that the FEM error is likely to be underestimated, since different implementations of the FEM converge to slightly different results. This underlines how critical the numerical accuracy is for these methods. For this reason, both approaches have been used here. The FDTD algorithm is an in-house code, graphically accelerated with subpixel smoothing [37]. The FEM method is implemented within the COMSOL commercial code.

Figure 7 compares the two methods by considering the convergence of the frequency of the fundamental order

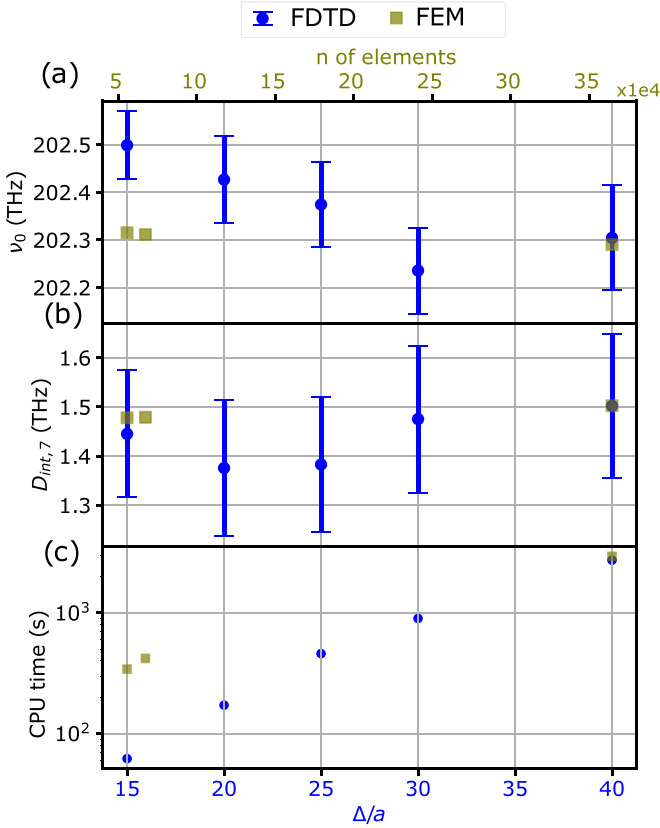


FIG. 7. Numerical solution of 3D ME with the nanobeam cavity: convergence of FEM (red) and FDTD (blue) methods against the number of elements and size of the grid, respectively; the error bar stands for the stochastic simulation on an ensemble of 20 realizations. (a) Fundamental mode frequency, (b) the integral dispersion up to the seventh-order mode, and (c) the CPU time in seconds.

mode v_0 [Fig. 7(a)] and the integrated dispersion up to the seventh-order mode [Fig. 7(b)] and the time required for the computation [Fig. 7(c)]. Let us note that the computation time scales with $(\Delta x/a)^4$ for the FDTD and moderately superlinearly with the number of elements used in the FEM; thus, the two horizontal scales cannot be compared directly. Moreover, a more reliable computation of the frequencies through FDTD is obtained by adding random fluctuations in the geometry (as discussed earlier), performing the calculation on 20 to 60 realizations (depending on the resolution) of the structure, and considering averages and standard deviations of the histograms of calculated frequencies. The standard deviation depends on the disorder introduced ($rms = 1$ nm), and it is not an estimate of a numerical accuracy. Thus, the time required by FDTD is much longer indeed if this method is used. Figure 7(a) shows that the inaccuracy for the frequency is about 10 GHz when FEM is used. More precisely, the accuracy is assessed by comparing the resonances computed by using either a low (67 252 elements) or a high (364 550 elements) resolution on the tetrahedral mesh, namely, $\sigma_{FEM}^2 = \frac{1}{N} \sum_m^N |\omega_{FEM,H,m} - \omega_{FEM,L,m}|^2$; hence, $\sigma_{FEM}/2\pi = 13$ GHz. As shown in Fig. 4, this is comparable to the average residual between the frequencies computed with our RM and with FEM. The FDTD converges to the same value with $a/\Delta x = 40$. The inaccuracy on the integrated

TABLE I. Workflow and overall performance of the method. The reduced model is built from the periodized structure (w_0). RM is updated by comparison with the 3D ME calculation (FEM) of the reference cavity (w_0 upd.). The profile is modified to one with flat dispersion as the target (w_1). RM is updated again against the 3D ME calculation of the optimized cavity (w_1 upd.). The geometry is optimized again with the updated model (w_2). σ_{RM} is the averaged residual between RM and 3D MEs, $\Delta^{(2)} = (N-2)^{-1} \sum_j \Delta_j^{(2)}$, where $\Delta_j^{(2)} = \omega_{j+1} + \omega_{j-1} - 2\omega_j$ is the averaged second-order dispersion, normalized to the FSR. Note that both the update and the optimization steps result in a minimization of two different figures of merit, i.e., σ_{RM} (blue arrows) and $\Delta^{(2)}$ (red arrows). The computing time for the 3D FDTD periodic and FEM calculations for w_0 , w_1 , and w_2 and the time needed to optimize the profile using the RM and the number of calls needed to converge are also shown.

	w_0	w_0 upd.	w_1	w_1 upd.	w_2
σ_{RM} (GHz)	200	→ 8	30	→ 12	13
$\Delta^{(2)}$ (%FSR)	27	31	→ 1.7	0.17	→ 0.12
3D ME	period.	w_0	w_1	w_2	
CPU time (s)	80314	2948	2776	2816	2816
fun. calls	–	723	220	557	254
CPU time (s)	–	356	107	261	125

dispersion [Fig. 7(b)] is similar, and it is matched by FDTD for $a/\Delta x = 30$. The two methods give almost identical results for $a/\Delta x = 40$. In terms of computing time (for a single FDTD realization) the resolution $a/\Delta x = 40$ corresponds to the high-resolution FEM mesh, while the low-resolution mesh corresponds to $a/\Delta x = 25$. With this resolution, we deduce from Figs. 7(a) and 7(b) that the error of the FDTD is about 100 GHz.

We conjecture that the accuracy of the RM may be better than that of the numerical solution of 3D MEs. As a matter of fact, the discretization of space through finite differences or finite elements results in uncorrelated deviations of the resonances. This source of randomness should vanish in the exact solution, and it may be much reduced in the RM since the method inherently averages out random deviations. However, the proof of this is problematic because of the accuracy limitation of numerical solutions. Still, our method guarantees that dispersion flatness remains within the order of 10 GHz in terms of the integrated dispersion, over the first seven confined modes, which is clearly better than what is achievable with the strictly bichromatic design that was reported in [8,11] or with the parabolic tapering design of Ref. [12]. Moreover, here we have shown how, by means of the RM, it is possible to tailor the dispersion of a wide class of resonators, regardless of their initial dispersion curves. Specifically, we could flatten the integrated dispersion of the highest-order modes by almost 3 orders of magnitude, i.e., from ≥ 1 THz down to ~ 10 GHz, by drastically changing the D_{int} curve.

3. The optimization algorithm: Workflow and performances

The performances of our method are summarized in Table I. Computation is performed using a 32-core CPU (AMD EPYC 7351) with clock frequency equal to 2.4 GHz and 64 GB RAM. The first step consists of establishing

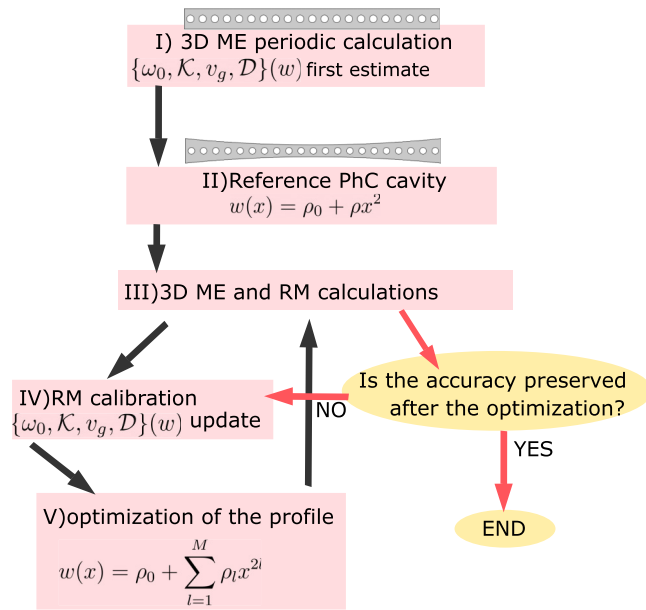


FIG. 8. Flowchart of the design algorithm: the band diagram calculation of a perfectly periodic structure (I) gives a first estimate of the structure parameters. A reference $w(x)$ PhC profile is taken into account (II) and numerically solved (III). After the calibration of the RM (IV), we proceed with the actual optimization (V). A loop across steps IV and V might be necessary if the accuracy is not sufficient upon optimization (red arrows).

the RM, which requires the calculation of the bands as a function of the control parameter (here w). This takes ~ 3000 s for each of the 26 values of w . The second step is the calculation of the frequencies for the reference cavity, as well as of the first and second optimized geometries, which each take about 3000 s using FEM. An error-minimization iterative procedure based on the steepest gradient is performed twice for updating the RM and twice for the optimization of the profile $w(x)$. Convergence requires a few hundred function calls, and the average time for evaluating the RM is 0.6 s. This gives a sense of the acceleration provided by replacing the solution of the 3D MEs with that of the RM.

In Fig. 8 we sketch a flowchart showing each step of our design technique: the initial step (I) consists of the band diagram calculation of a perfectly periodic structure for different values of the control parameter. A first estimate of the structure parameters and of their dependence on w can be extrapolated by means of a polynomial fit, as sketched in Fig. 3. Consequently, a reference profile of $w = \rho_0 + \rho x^2$ is taken into account (II), and the structure is solved by means of both RM and 3D ME solvers (III). At this point, the RM is calibrated, and the set $\{\omega_0, \mathcal{K}, v_g, \mathcal{D}\}(w)$ is updated to recover the best accuracy (IV). The following step is the actual optimization of the $\rho_{i|i>0}$ coefficients of an even M th-order polynomial expansion $w(x) = \rho_0 + \sum_{l=1}^M \rho_l x^{2l}$ (V). After the optimization cycle, it is essential to verify whether the RM accuracy was degraded (red arrows): if so, another loop of steps IV and V will be needed in order to recover the prescribed accuracy.

- [1] R. W. Boyd, *Nonlinear Optics* (Elsevier, Amsterdam, 2020)
- [2] T. J. Kippenberg, A. L. Gaeta, M. Lipson, and M. L. Gorodetsky, Dissipative Kerr solitons in optical microresonators, *Science* **361**, eaan8083 (2018).
- [3] S. Matsuo, A. Shinya, T. Kakitsuka, K. Nozaki, T. Segawa, T. Sato, Y. Kawaguchi, and M. Notomi, High-speed ultracompact buried heterostructure photonic-crystal laser with 13 fJ of energy consumed per bit transmitted, *Nat. Photonics* **4**, 648 (2010).
- [4] G. Crosnier, D. Sanchez, S. Bouchoule, P. Monnier, G. Beaudoin, I. Sagnes, R. Raj, and F. Raineri, Hybrid indium phosphide-on-silicon nanolaser diode, *Nat. Photonics* **11**, 297 (2017).
- [5] Y. Yu, W. Xue, E. Semenova, K. Yvind, and J. Mork, Demonstration of a self-pulsing photonic crystal Fano laser, *Nat. Photonics* **11**, 81 (2017).
- [6] K. Nozaki, S. Matsuo, T. Fujii, K. Takeda, A. Shinya, E. Kuramochi, and M. Notomi, Femtofarad optoelectronic integration demonstrating energy-saving signal conversion and nonlinear functions, *Nat. Photonics* **13**, 454 (2019).
- [7] Y. Takahashi, Y. Inui, M. Chihara, T. Asano, R. Terawaki, and S. Noda, A micrometre-scale Raman silicon laser with a microwatt threshold, *Nature (London)* **498**, 470 (2013).
- [8] G. Marty, S. Combri , F. Raineri, and A. De Rossi, Photonic crystal optical parametric oscillator, *Nat. Photonics* **15**, 53 (2021).
- [9] J. R. Stone, G. Moille, X. Lu, and K. Srinivasan, Conversion Efficiency in Kerr-Microresonator Optical Parametric Oscillators: From Three Modes to Many Modes, *Phys. Rev. Applied* **17**, 024038 (2022).
- [10] Y. Sun, S. Combri , F. Bretenaker, and A. De Rossi, Mode Locking of the Hermite-Gaussian Modes of a Nanolaser, *Phys. Rev. Lett.* **123**, 233901 (2019).
- [11] S. Combri , G. Lehoucq, G. Moille, A. Martin, and A. De Rossi, Comb of high-Q resonances in a compact photonic cavity, *Laser Photonics Rev.* **11**, 1700099 (2017).
- [12] G. Marty, S. Combri , A. De Rossi, and F. Raineri, Hybrid InGaP nanobeam on silicon photonics for efficient four wave mixing, *APL Photonics* **4**, 120801 (2019).
- [13] M. Clementi, A. Barone, T. Fromherz, D. Gerace, and M. Galli, Selective tuning of optical modes in a silicon comb-like photonic crystal cavity, *Nanophotonics* **9**, 205 (2019).
- [14] J. S. Jensen and O. Sigmund, Topology optimization for nanophotonics, *Laser Photonics Rev.* **5**, 308 (2011).
- [15] S. Molesky, Z. Lin, A. Y. Piggott, W. Jin, J. Vuckovi , and A. W. Rodriguez, Inverse design in nanophotonics, *Nat. Photonics* **12**, 659 (2018).
- [16] M. Minkov, I. A. Williamson, L. C. Andreani, D. Gerace, B. Lou, A. Y. Song, T. W. Hughes, and S. Fan, Inverse design of photonic crystals through automatic differentiation, *ACS Photonics* **7**, 1729 (2020).
- [17] T. W. Hughes, M. Minkov, I. A. Williamson, and S. Fan, Adjoint method and inverse design for nonlinear nanophotonic devices, *ACS Photonics* **5**, 4781 (2018).
- [18] C. T. Santis, S. T. Steger, Y. Vilenchik, A. Vasilyev, and A. Yariv, High-coherence semiconductor lasers based on integral

- high-q resonators in hybrid Si/III-V platforms, *Proc. Natl. Acad. Sci. USA* **111**, 2879 (2014).
- [19] T. Asano, Y. Ochi, Y. Takahashi, K. Kishimoto, and S. Noda, Photonic crystal nanocavity with a Q factor exceeding eleven million, *Opt. Express* **25**, 1769 (2017).
- [20] M. Notomi, T. Tanabe, A. Shinya, E. Kuramochi, H. Taniyama, S. Mitsugi, and M. Morita, Nonlinear and adiabatic control of high-q photonic crystal nanocavities, *Opt. Express* **15**, 17458 (2007).
- [21] Q. Quan and M. Loncar, Deterministic design of wavelength scale, ultra-high q photonic crystal nanobeam cavities, *Opt. Express* **19**, 18529 (2011).
- [22] A. Bazin, R. Raj, and F. Raineri, Design of silica encapsulated high-q photonic crystal nanobeam cavity, *J. Lightwave Technol.* **32**, 952 (2014).
- [23] Y. Akahane, T. Asano, B.-S. Song, and S. Noda, High-Q photonic nanocavity in a two-dimensional photonic crystal, *Nature (London)* **425**, 944 (2003).
- [24] F. Wang, R. E. Christiansen, Y. Yu, J. Mørk, and O. Sigmund, Maximizing the quality factor to mode volume ratio for ultra-small photonic crystal cavities, *Appl. Phys. Lett.* **113**, 241101 (2018).
- [25] B.-H. Ahn, J.-H. Kang, M.-K. Kim, J.-H. Song, B. Min, K.-S. Kim, and Y.-H. Lee, One-dimensional parabolic-beam photonic crystal laser, *Opt. Express* **18**, 5654 (2010).
- [26] I. Ghorbel, F. Swiadek, R. Zhu, D. Dolfi, G. Lehoucq, A. Martin, G. Moille, L. Morvan, R. Braive, S. Combri , and A. De Rossi, Optomechanical gigahertz oscillator made of a two photon absorption free piezoelectric III/V semiconductor, *APL Photonics* **4**, 116103 (2019).
- [27] P. Yu and M. Cardona, *Fundamentals of Semiconductors: Physics and Materials*, Advanced Texts in Physics (Springer, Berlin, 2005), Vol. 3.
- [28] A. Yariv, *Quantum Electronics* (Wiley, New York, 1989).
- [29] A. Aceves and S. Wabnitz, Self-induced transparency solitons in nonlinear refractive periodic media, *Phys. Lett. A* **141**, 37 (1989).
- [30] A. De Rossi, C. Conti, and S. Trillo, Stability, Multistability, and Wobbling of Optical Gap Solitons, *Phys. Rev. Lett.* **81**, 85 (1998).
- [31] P. Colman, C. Husko, S. Combri , I. Sagnes, C. W. Wong, and A. De Rossi, Temporal solitons and pulse compression in photonic crystal waveguides, *Nat. Photonics* **4**, 862 (2010).
- [32] S. Malaguti, G. Bellanca, S. Combrie, A. de Rossi, and S. Trillo, Temporal Gap Solitons and All-Optical Control of Group Delay in Line-Defect Waveguides, *Phys. Rev. Lett.* **109**, 163902 (2012).
- [33] J. R. de Lasson, L. H. Frandsen, P. Gutsche, S. Burger, O. S. Kim, O. Breinbjerg, A. Ivinskaya, F. Wang, O. Sigmund, T. H yrynen, A. V. Lavrinenko, J. M rk, and N. Gregersen, Benchmarking five numerical simulation techniques for computing resonance wavelengths and quality factors in photonic crystal membrane line defect cavities, *Opt. Express* **26**, 11366 (2018).
- [34] R. Courant, E. Isaacson, and M. Rees, On the solution of nonlinear hyperbolic differential equations by finite differences, *Comm. Pure Appl. Math.* **5**, 243 (1952).
- [35] S. V. Patankar, *Numerical Heat Transfer and Fluid Flow*, 1st ed. (CRC Press, Boca Raton, 1980).
- [36] J. Bezanson, A. Edelman, S. Karpinski, and V. B. Shah, Julia: A fresh approach to numerical computing, *SIAM Rev.* **59**, 65 (2017).
- [37] A. F. Oskooi, C. Kottke, and S. G. Johnson, Accurate finite-difference time-domain simulation of anisotropic media by subpixel smoothing, *Opt. Lett.* **34**, 2778 (2009).